Nanoscale

PAPER

View Article Online
View Journal | View Issue

Cite this: *Nanoscale*, 2020, **12**, 1580

Atomic-scale tuning of oxygen-doped $Bi_2Te_{2.7}Se_{0.3}$ to simultaneously enhance the Seebeck coefficient and electrical conductivity†

Shuankui Li,[a] Mihai Chu,[a] Weiming Zhu,[a] Rui Wang,[a] Qi Wang,[b] Fusheng Liu,[c] Meng Gu, *[b] Yinguo Xiao*[a] and Feng Pan *[a]

Received 3rd September 2019,
Accepted 26th November 2019

DOI: 10.1039/c9nr07591g

rsc.li/nanoscale

Manipulation of oxygen-related impurities is an extreme challenge for most of the thermoelectric materials, especially for those possessing nanostructures, since they normally result in the degradation of the thermoelectric performance. Here, we demonstrate that by atomic-scale controlling of oxygen doping in the form of dislocation clusters in $Bi_2Te_{2.7}Se_{0.3}$ (BTS) thermoelectric materials, the trade-off between the Seebeck coefficient and electrical conductivity is broken, resulting in the simultaneously enhanced Seebeck coefficient and electrical conductivity and the suppressed thermal conductivity. As a consequence, a maximum ZT of 0.91 is achieved, which is approximately 1.4 times higher than that of pristine BTS. Based on HR-STEM investigation, the oxygen-related dislocation clusters can be unambiguously identified and we argue that the optimized carrier/phonon transport behavior can be attributed to the multifunctionality of oxygen-related dislocation clusters in BTS acting as electron donors, electron energy filters and phonon blockers. Our work provides a clear microscopic understanding on the role of oxygen doping in modifying phonon/carrier transport behavior in BTS thermoelectric materials, which provides an efficient avenue for designing high performance thermoelectric materials.

Introduction

Thermoelectric (TE) materials, which can harvest useful electrical power from waste heat, have attracted considerable attention since more than 50% of the world's energy consumption is wasted in the form of heat.[1,2] The efficiency of TE conversion is defined by a dimensionless figure of merit $ZT = S^2\sigma T/\kappa$, where S, σ, κ, and T are the Seebeck coefficient, electrical conductivity, thermal conductivity, and absolute temperature, respectively.[3,4] For real thermoelectric materials, two main strategies are usually adopted to enhance zT: one is to reduce the lattice thermal conductivity (κ_{latt}) by phonon engineering[5,6] and the other is to enhance the power factor ($S^2\sigma$) by band engineering.[7] Various approaches have been adopted to improve the performance of the TE material, such as traditional doping and nanostructure engineering.[8,9] However, for almost all of the TE materials, oxygen-related impurities are an extremely common concern, especially for those possessing nanostructures, because they normally result in the degradation of the TE performance.[10] The most common condition is the formation of oxide particles due to surface oxidation, which often lead to the significant reduction of σ for most of the thermoelectric materials.[10,11–13] Few experimental studies have been performed to explore the influence of oxygen-related impurities on the carrier/phonon transport behaviour in bulk thermoelectric materials, because it is difficult to have precise control over the oxygen-related impurities in the sample.

A Bi_2Te_3-based alloy is considered to be a promising thermoelectric candidate in the room temperature region. Structurally, Bi_2Te_3 can be viewed as a layered material consisting of stacked quintuple layers Te(1)–Bi–Te(2)–Bi–Te(1) along the c-axis bonded together by weak van der Waals interactions.[14–16] It is reported that Se has complete solubility in Bi_2Te_3 with a preferential occupancy at two different Te sites, with increasing Se concentrations. In the case of $Bi_2Te_{2.7}Se_{0.3}$, more electronegative Se atoms occupy Te(2) sites as compared to Bi_2Te_3.[17] The enhancement of the TE performance of Bi_2Te_3-based alloys is mainly realized by nanostructure engineering, which is effective in the reduction of κ_{latt} but usually harmful to σ simultaneously.[18–21] Generally, for the

[a]School of Advanced Materials, Peking University Shenzhen Graduate School, Shenzhen, 518055, China. E-mail: y.xiao@pku.edu.cn, panfeng@pkusz.edu.cn
[b]Department of Materials Science and Engineering & Shenzhen Engineering Research Center for Novel Electronic Information Materials and Devices, Southern University of Science and Technology, Shenzhen 518055, China. E-mail: gum@sustc.edu.cn
[c]College of Materials Science and Engineering, Shenzhen University and Shenzhen Key Laboratory of Special Functional Materials, Shenzhen, 518060, China

†Electronic supplementary information (ESI) available. See DOI: 10.1039/c9nr07591g

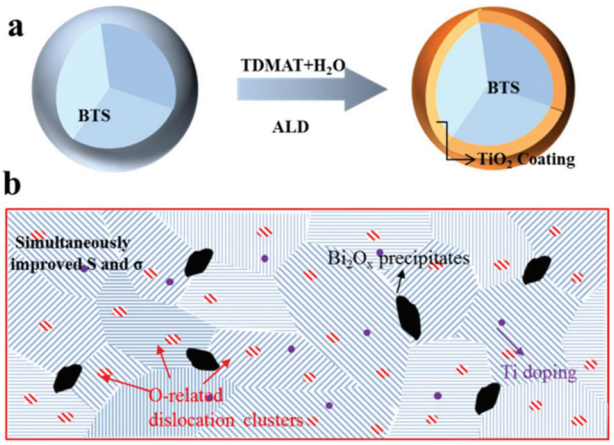

Fig. 1 A schematic of controlling the oxygen doping in BTS thermoelectric materials *via* an ALD-based solid phase diffusion strategy. (a) Introduction of an utrathin TiO_2 layer on the BTS powder surface. (b) Schematic of the microstructure of the bulk sample.

nanostructured powders prepared using bottom-up approaches, the appearance of oxygen-related impurities is inevitable, which normally hampers σ and results in the degradation of the TE performance.[10,11] However, it is difficult to investigate the influence of oxygen-related impurities on carrier/phonon transport behaviour experimentally. Inspired by our previous work on grain boundary engineering,[22] we attempt to accurately control the oxygen-related impurities in BTS using an ALD-based solid phase diffusion strategy, and investigate the related carrier/phonon transport behavior.

Herein, we propose a novel ALD-based solid phase diffusion strategy to accurately control the oxygen-related impurities in BTS, and investigate the related electron/phonon transportation behaviour (Fig. 1). We found that the trade-off between S and σ could be broken *via* accurately controlling oxygen doping in the form of dislocation clusters. The simultaneous enhancement of S (~10%) and σ (~10%) could be achieved, which can be ascribed to the donor-like effect and the energy filtering effect of O-related dislocation clusters. Moreover, the O-related dislocation clusters, large-scale lattice distortion, and stress and strain together with nano-scale Bi_2O_x precipitates contribute to the low κ_{latt} (0.33 W m^{-1} K^{-1}) of the ALD-coated samples. A maximum ZT of 0.91 is obtained, approximately 1.4 times higher than that of the BTS matrix. This work provides an effective strategy to enhance thermoelectric performance through simultaneously improving electrical and thermal transport properties.

Experimental section

Preparation of ALD-coated BTS

A BTS matrix was synthesized using a solution-synthesis strategy as described in our previous report.[22] A TiO_2 layer was coated on the surface of the BTS matrix in a homemade continuous-flow ALD reactor operated under a base pressure of ~1 Torr. Typically, the TiO_2 layer was deposited using tetrakisdimethylamido-titanium (TDMAT) and H_2O as ALD precursors at 150 °C. The bubbler containing TDMA was heated to 40 °C and the delivery line was heated to 70 °C. The precursor dose and purge time were 30 seconds and 60 seconds, respectively. Ar gas served as both a carrier and a purging gas.

Characterization

X-ray powder diffraction (XRD) measurement was performed on a Bruker D8 Advance X-ray diffractometer; field-emission scanning electron microscopy (FE-SEM) analysis of morphology is carried out on a Zeiss SUPRA-55 microscope integrated with Oxford EDS; X-ray photoelectron spectra (XPS) were acquired on a Thermo Fisher ESCALAB 250X surface analysis system equipped with a monochromatized Al anode X-ray source (X-ray photoelectron spectroscopy, XPS, $h\nu$ = 1486.6 eV). A focused ion beam system (FIB; JIB 4601F, JEOL) was used to prepare the TEM sample from the bulk sample. The overall morphology and detailed crystallographic information were deduced from high-resolution field-emission transmission electron microscopy (FETEM; JEOL-3200FS, 300 kV). The STEM analysis is performed using a double-Cs-aberration corrected Themis G2 microscope at 300 kV with super-X EDS detectors.

Thermoelectric measurements

The BTS powders were pressed into pellets by hot pressed (HP) sintering at 623 K for 1 h under vacuum with a uniaxial pressure of 60 MPa. The pellets were cylinders with 10 mm in diameter and 12 mm in height. The disk with a thickness of around 2 mm was cut from the sintered pellets to measure the thermal conductivity, and a cuboid about 3 mm × 3 mm × 10 mm was cut to measure the σ and S. The electrical conductivity and Seebeck coefficient were measured using an ULVAC ZEM-3 within the temperature range 300–500 K. The total thermal conductivity (κ_{tot}) was calculated through $\kappa_{tot} = DC_p\rho$, where D, C_p, and ρ are the thermal diffusivity coefficient, specific heat capacity, and density, respectively. The thermal diffusivity coefficient was measured on a laser flash apparatus using a Netzsch LFA 467 from 300 to 500 K, and the specific heat (C_p) was examined using a differential scanning calorimeter (Mettler DSC1), and the density (ρ) was calculated by using the mass and dimensions of the pellet.

Results and discussion

The grain boundary engineering based on the ALD strategy provides a novel approach to optimize the dimension and composition of the grain boundary. As dominating thermoelectric materials for industrial applications, Bi_2Te_3-based solid solutions provide an excellent model system for systematic study on the microstructure-related transport properties of carriers and phonons, which has been investigated tentatively in our previous work.[23,24] BTS nanoparticles were first synthesized *via* a solution-based strategy, and the XRD pattern

can be indexed to hexagonal BTS (space group *I*2/*b*, PDF 01-074-4893).[22] Then, the utrathin TiO_2 layer was introduced to the surface of BTS nanoparticles using the ALD method. After 10-ALD-cycle coating, the XRD pattern did not show any crystalline peak originating from the TiO_2 layer because the TiO_2 layer is amorphous and the thickness is less than 1 nm (Fig. 2a). In order to characterize the ultrathin TiO_2 layer, XPS analysis was performed. As shown in Fig. 2b, the emergence of the Ti 2p peak confirms the formation of an ultrathin TiO_2 layer on the BTS surface. The O 1s region shows the O^{2-} peak at 530 eV originating from the surface oxidation of BTS and the TiO_2 layer, and the shoulder located at 531.6 eV related to the surface hydroxyl OH and/or carbonate species. The TEM images (Fig. 2d and e) confirmed the presence of a ~1 nm uniform and smooth TiO_2 layer; this is consistent with the amorphous characteristic of an ALD film. It is noted that the interface between the TiO_2 layer and BTS is well-defined, which illustrates that BTS is stable during the ALD process due to a low reaction temperature (150 °C). EDS mapping (Fig. 2f) reveals a uniform distribution of Ti and oxygen elements in the ALD-coated BTS nanoparticles, and it also confirms the formation of the ultrathin TiO_2 layer.

Compared to other thin film deposition techniques, ALD has a lot of advantages, particularly its precise thickness control at the atomic scale.[25–27] Firstly, TiO_2 films were deposited on silicon wafers to determine the growth per cycle (GPC). As shown in Fig. S1a,† the thickness of the TiO_2 film increases linearly with the number of ALD cycles, and the GPC estimated from the slope of the fitted linear function is about 0.7 Å per cycle. AFM characterization demonstrates the high uniformity of the TiO_2 films, which is consistent with the result observed by TEM (Fig. S1b†). As expected, the thickness of the TiO_2 layer on the BTS surface is about 2 nm, 4 nm and 8 nm for the BTS samples after 30, 50 and 90 ALD cycles, respectively (Fig. S1c–f†). The growth rate of TiO_2 coating on the BTS surface was around 0.8 Å per ALD cycle, in agreement with the result observed on the silicon wafers. All the above results indicate that the thickness of TiO_2 coating can be controlled at the nanoscale, which is significantly better than the conventional solution-based interface treatment strategy.

The as-prepared ALD-coated BTS sample was pressed into bulk by hot-pressed sintering at 623 K. The XRD patterns of the bulk samples match well with the standard peaks and no additional peak is detected (Fig. S2†). To understand the oxygen diffusion behavior, the microstructures were investigated *via* various electron microscopy studies. The low magnification STEM-HAADF images (Fig. S3b†) demonstrate that the BTS grains with an average size of about 500 nm are closely packed, which is in agreement with the high density (>97%) of the as-prepared bulk samples (Table S1†). The corresponding EDS spectrum confirmed the existence of oxygen elements in the sample (Fig. S3c†). Surprisingly, the EDS characterization studies of the bulk sample reveal negligible Ti content, which might be attributed to the uniform distribution of Ti element in the sample. In the ideal case, considering the sphere BTS grains (500 nm) surrounded by an about 5 nm TiO_2 layer, the volume fraction of TiO_2 is only about 1.2%, which is lower in the real samples because of the aggregation of BTS nano-

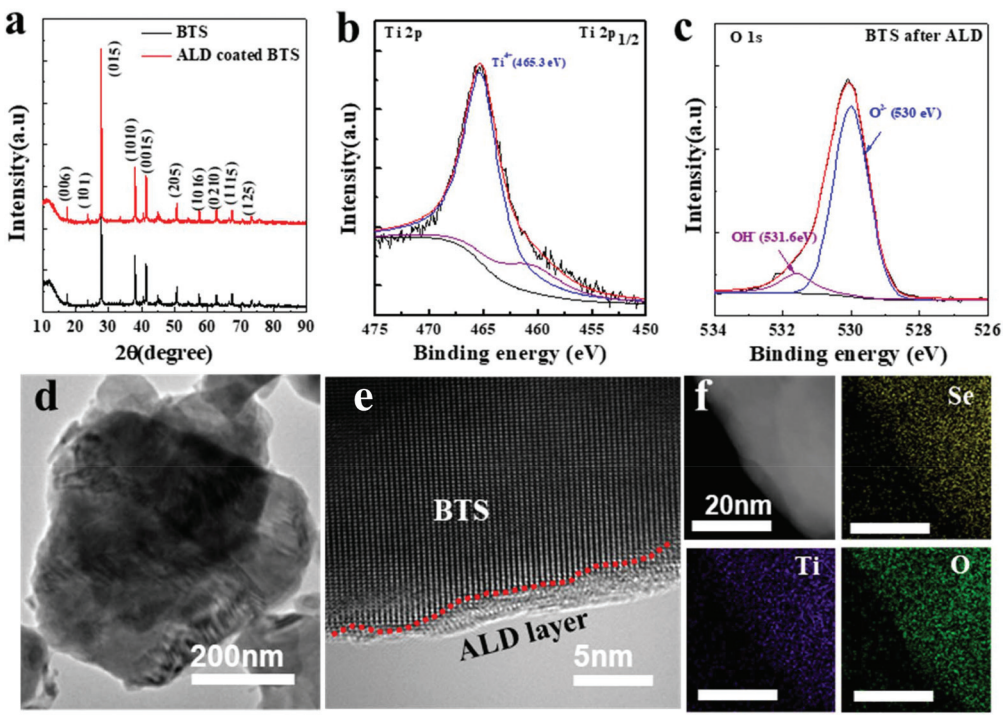

Fig. 2 (a) XRD pattern of the BTS matrix and ALD-coated BTS. XPS spectra for the as-prepared ALD-coated BTS sample. (b) Ti 2p peak and (c) O 1s peak. (d) TEM, (e) HRTEM image and (f) EDS mapping of the S10 sample.

particles. Thus, for the case that the Ti element is homogeneously distributed in the BTS grains, the maximum Ti element content is only about 0.35 wt%, which is almost beyond the detection limit of EDS. Differently, the O element in the sample is inhomogeneous, in which some O-rich precipitates are embedded in the BTS matrix (Fig. S3d†) and their chemical composition is estimated to be Bi_2O_x revealed by EDS mapping. Surrounding the Bi_2O_x precipitates, some Te secondary phase can be observed, which suggests that a small amount of oxygen atoms may occupy the Te sites. Moreover, XPS is used to characterize the composition of the as-prepared bulk sample. In the O 1s spectra (Fig. S3a†), the O^{2-} peak at 530 eV and a shoulder located at 531.6 eV are all observed. Remarkably, a new peak with a lower binding energy (529.5 eV) appeared, which may originate from oxygen atoms of the O-related dislocation clusters in the Bi_2Te_3 matrix.[10,28] These results agree with our speculation that O existed in the sample in the form of large-scale Bi_2O_x precipitates and O-related dislocation clusters, which is firmly confirmed by the TEM results. Moreover, in the Ti 2p spectra, a clear shoulder at a lower binding energy assigned to Ti^{3+} can be seen, which suggested there is a small number of Ti ions taking up Bi positions in the BTS. On the basis of the above discussion, we conclude that the oxygen atoms of the TiO_2 layer could diffuse from the grain boundaries to the Bi_2Te_3 matrix during the sintering process, which could be used to optimize the carrier/phonon transport behaviour.

Unveiling of the microstructure of the bulk sample was further conducted by various electron microscopy techniques. Fig. 3a reveals that the sample is composed of approximately 200–500 nm BTS grains. There are some Bi_2O_x precipitates embedded on the grain boundaries of the BTS matrix as mentioned previously, which may originate from the reaction between the TiO_2 layer and the BTS matrix during the sintering

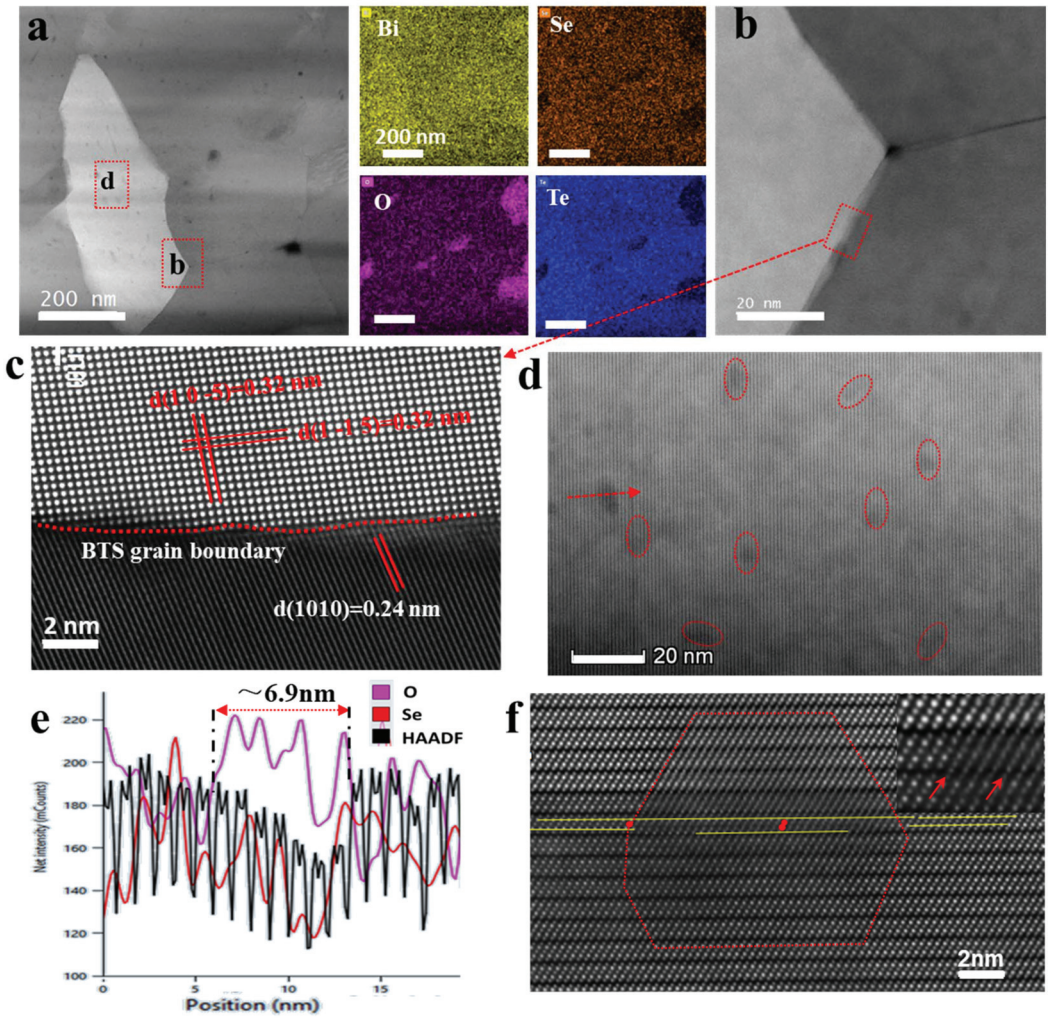

Fig. 3 Cross-sectional scanning of STEM images and elemental mapping of the bulk sample. (a) Typical low-magnification HAADF-STEM image and the corresponding EDS elemental maps. (b) HAADF-STEM image of the selected grain boundary observed in (a). (c) HAADF-STEM image (taken along the [5 10 1] axis of the upper BTS grain) of the grain boundary. (d) HAADF-STEM image of the red rectangular region in (a). (e) Elemental line scanning and (f) the HAADF-STEM image (taken along the *a*-axis of BTS) of the O-related dislocation cluster area observed in (d).

process. The BTS grain boundary with a coherent feature is clearly observed in the HAADF-STEM image (Fig. 3b and c), which could effectively scatter the heat-carrying phonons. The EDX images reflect composition homogeneity (Fig. S4†) at the BTS grain boundaries, which confirms that the TiO_2 layer could react with the BTS matrix during the sintering process. Besides the large-scale Bi_2O_x precipitates, high density dislocation clusters can be observed on the BTS grain (Fig. 3d), which exhibit large mismatch with the lattice structure of BTS. The EDX line scanning in Fig. 3e clearly demonstrates that the dislocation cluster regions are O-rich. Moreover, the microstructure of the pure BTS sample is investigated for comparison, which can exclude the existence of oxygen-related dislocation clusters in the pure BTS sample (Fig. S5†), and firmly confirms that the oxygen impurity originates from the introduced utrathin TiO_2 layer. In accordance with the experimental observation, it can be deduced that a small amount of oxygen atoms diffuses into the BTS crystal lattice during sintering, which leads to the formation of high-density O-related dislocation clusters. It is noted that in contrast to ordinary dislocation, the size of O-related dislocation clusters is around 7 nm which lies between the size of ordinary dislocation and nanoprecipitates (Fig. 3e and f).

The O-related dislocation clusters accompanied by large-scale lattice distortion in the BTS grain can be treated as charged Coulomb scattering centers, which will draw forth the enhancement of S by the energy filtering effect. As mentioned above, the O-related dislocation clusters in the BTS grain would lead to the generation of Te vacancies, which can donate electrons and pull the Fermi energy up to higher levels, giving rise to a positive influence on the n-type conductivity. Thus, due to the diffusion of O during the sintering process, grain boundary reconstruction occurred during sintering, and the high-density O-related dislocation clusters could be introduced to the BTS grain, which could be used to optimize the carrier/phonon transport behaviour. Moreover, previous research indicates that Ti doping at the concentration of 1.4×10^{17} in the Bi_2Te_3 could harm the electrical conductivity and thermoelectric performance, which is in contrast to our experimental results that the Seebeck coefficient and electrical conductivity simultaneous enhanced.[28] This fact may be ascribed to the ultralow concentration of Ti doping in our sample, which results in a negligible effect on the carrier/phonon transport behavior. Hence, in the present sample, the oxygen impurity appears in the form of large sized Bi_2O_x and O-related dislocation clusters in the BTS matrix grain, which plays a key role in optimizing the thermoelectric parameters.

The thermoelectric properties of the samples with different thicknesses of ALD coating are plotted, as shown in Fig. 4. The σ decreases with temperature for all the samples, exhibiting the typical degenerate-semiconductor behavior (Fig. 4a). The values of σ (~573 S cm^{-1} at 300 K) and S (−158.3 μV K^{-1}) of

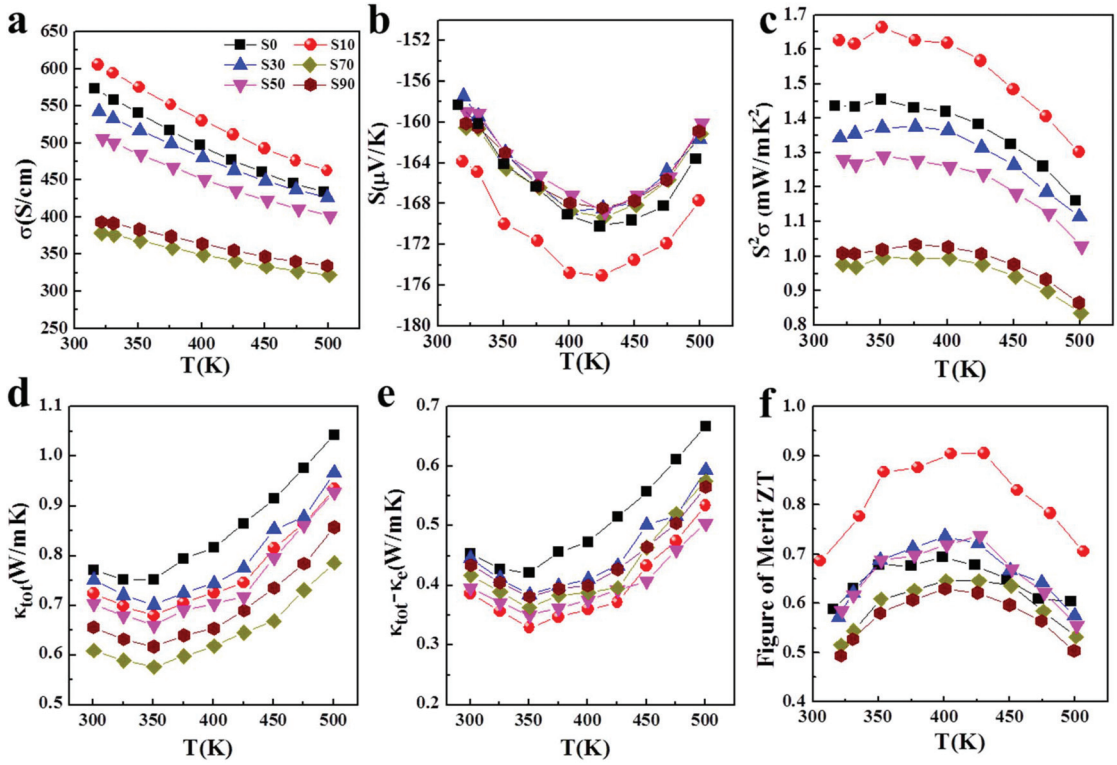

Fig. 4 The thermoelectric transport properties of the BTS sample after different ALD cycles. (a) Electrical conductivity (σ), (b) Seebeck coefficient (S), (c) power factor ($S^2\sigma$). (d) Total thermal conductivity (κ_{tot}), (e) the lattice and bipolar thermal conductivity calculated by subtracting the electronic thermal conductivity (κ_e) from the total thermal conductivity. (f) Thermoelectric figure of merit ZT.

pure BTS are comparable to that of reported Bi_2Te_3-nanostructured bulk materials.[29] However, for S10 with only about 1 nm ultrathin ALD coating, the σ (~10%) and S (~10%) simultaneously increased, which can be ascribed to the donor-like effect and the energy filtering effect of O-related dislocation clusters. These clusters in the BTS grain would lead to the generation of Te vacancies, which can donate electrons and pull the Fermi energy up to higher levels, leading to a positive influence on the n-type conductivity. This donor-like effect of O-related dislocation clusters is further confirmed by the slightly increased electron concentration (5.3×10^{19} cm^{-3}) of S10. In S10, the O defects mainly exist in the form of O-related dislocation clusters, which make the simultaneous enhancement of S and σ possible. The phenomenon is unusual, because in most cases, S decreases and σ increases along with increasing n.[30,31] In general, as n increases, the E_F moves deeper into the band where the density of states is flatter, hence reducing the entropy carried by charges around E_F. The simultaneous enhancement of S and σ is only observed for S10 with high density O-related dislocation clusters, suggesting that optimizing oxygen doping is crucial to improve the properties of carrier transport. These findings demonstrate that atomic-scale tuning of oxygen doping is achieved, which could be used to optimize the carrier transport behavior.

According to the relaxation time model,[32,33] S can be expressed as follows:

$$|S| \approx \frac{k_B}{e} \cdot \frac{\pi^2}{3} \cdot \frac{k_B T}{E_F} \cdot \left(\frac{3}{2} + r\right)$$

where E_F is the Fermi level, r is the index of the electron relaxation time, and k_B and e are the Boltzmann constant and elementary charge, respectively. For traditional TE materials, the S decreases with increasing n, which leads to the conventional wisdom of the inverse coupling between S and σ. However, the increased r also contributes to the enhanced S, which allows the breaking of the coupling between S and σ, as in our case. For S10, O-related dislocation clusters as ionized doping may cause a transition of the scattering mechanism from phonon-dominated ($r = -1/2$) to more impurity-dominated transport behaviour ($r = 3/2$), similar to the effect of native defects in Bi_2Te_3 as reported by Joonki Suh *et al.*[34] The O-related dislocation clusters enabled decoupling of S and σ which resulted in an enhanced power factor for S10. As a result, a high power factor about 1.68 mW m^{-1} K^{-2} is obtained (Fig. 4c), which shows 30% enhancement compared with BTS (1.45 mW m^{-1} K^{-2}). As the thickness of ALD coating increased, the main form of oxygen impurities in the sample transformed from O-related dislocation clusters to nanoscale Bi_2O_x precipitates due to the low solid solubility of oxygen in BTS. Obviously, the formation of large-scale Bi_2O_x precipitates has a negative effect on σ, which is quite similar to the case of surface oxidation.[10,11] For the thermoelectric composites, the energy-filtering effect is mainly related to the potential barriers, and the optimum potential barrier height should be close to k_BT or somewhat higher.[35,36] However, for the BTS–Bi_2O_x system, the barrier height (about 1.0 eV) is far greater than k_BT, which has a negative effect on the carrier transport properties. As shown in the above scenario, by adjusting the thickness of ALD coating at the atomic scale, either Bi_2O_x precipitates or O-related dislocation clusters in the sample can be formed selectively.

As expected, the thermal conductivities of the ALD-coated samples were significantly lower than those of the BTS matrix, due to effective phonon scattering at grain boundaries and introduced oxygen impurities. For the TE semiconductors, the total thermal conductivity (κ_{tot}) can be expressed as $\kappa_{tot} = \kappa_e + \kappa_{latt} + \kappa_{bi}$, in which κ_e is the electronic thermal conductivity ($\kappa_{el} = L\sigma T$, $L = 1.5 + \exp(-|S|/116)$), κ_{latt} is the lattice thermal conductivity, and κ_{bi} is the bipolar thermal conductivity. To calculate the κ_{tot}, the C_p of the present $Bi_2Te_{2.7}Se_{0.3}$ bulk samples is measured (Fig. S5†). It is found that the C_p is slightly lower than the Dulong–Petit value and higher than the previously reported value for the same compositions.[37,38] It is noted that in the low temperature region ($T < 350$ K), the contribution of κ_{bi} could be ignored, and κ_{latt} could be obtained by subtracting κ_e from κ_{tot}. It is found that the κ_{latt} of the BTS (0.46 W m^{-1} K^{-1}) is comparable to that of the previously reported results.[17,22–24] After introducing oxygen impurities, the κ_{latt} can be effectively suppressed. Typically, the κ_{latt} at room temperature for the BTS decreases from 0.46 W m^{-1} K^{-1} to 0.39 W m^{-1} K^{-1} and 0.43 W m^{-1} K^{-1} for S10 and S90, respectively. It is observed that S10 exhibits much lower κ_{latt} than S90, despite the high content of oxygen impurities in the latter. These results indicate that phonon scattering is closely related to the form of oxygen impurities in the sample. The synergistic effect between O-related dislocation clusters, large-scale lattice distortion, the stress and strain and Bi_2O_x precipitates may enhance the phonon scattering of full-wavelength, which contributes to the low κ_{latt} of S10. In the high temperature range ($T > 350$ K), the bipolar contribution became significant (Fig. S6†). It is found that the bipolar contribution to the thermal conductivity was lower in the ALD-coated samples than in the pure BTS sample, which may be attributed to the scattering of minority carriers at oxygen impurities and grain boundaries.[20]

To understand the phonon scattering effect of the oxygen impurities in the sample, detailed characterization studies on the microstructure for samples S10 and S70 are further conducted. It can be observed that the morphology of S10 is significantly different from that of S70 (Fig. 5a and b). Clearly, in S10, high density O-related dislocation clusters can be observed almost in all grains, and the dislocation density is estimated to be around 1×10^{12} cm^{-2}. It is should be noted that in contrast to conventional dislocation, the O-related dislocation clusters caused large-scale lattice distortion of the BTS matrix with about 7 nm in size, which lies between the ordinary dislocation and the second phase. Due to the existence of O-related dislocation clusters and large-scale lattice distortion, the stress and strain in S10 will be noticeably larger, which could enhance the medium and short wavelength phonon scattering.[37] In contrast, large-scale Bi_2O_x precipitates can be observed in S70 (indicated by the dotted oval

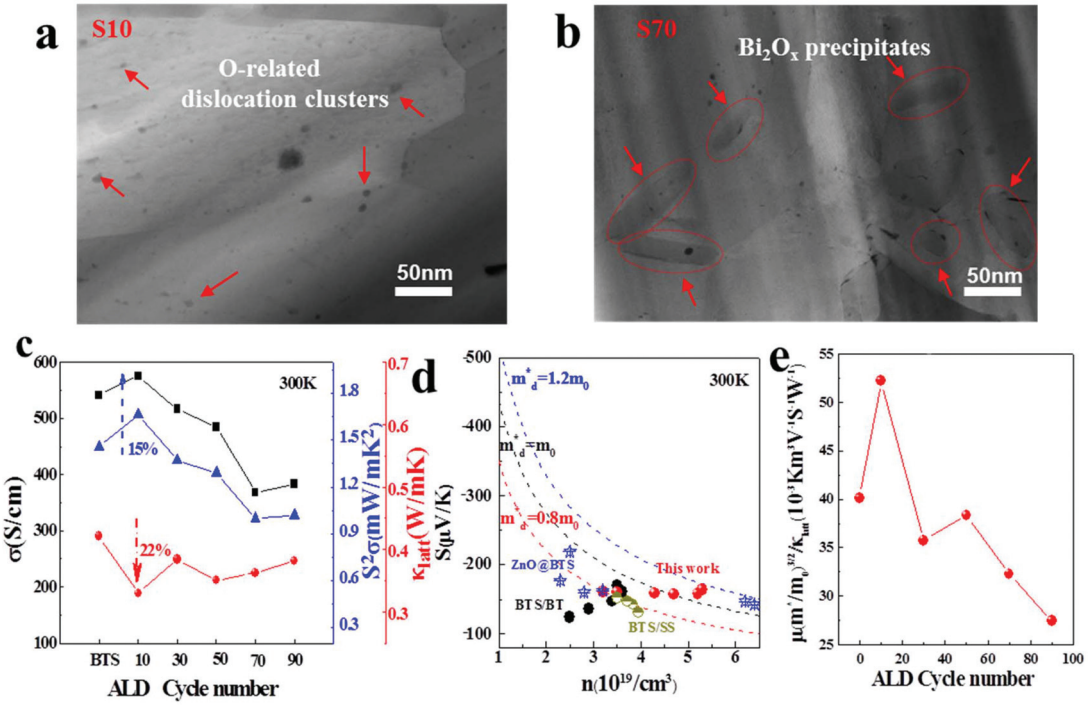

Fig. 5 The low magnified STEM image of the bulk sample of (a) S10 and (b) S70. (c) The electrical conductivity, lattice thermal conductivity and power factor at 300 K. (d) Seebeck coefficient (S) as a function of carrier concentration (n) and (e) $\mu(m^*/m_0)^{3/2}/\kappa_{latt}$ of all the ALD-coated BTS samples as a function of ALD cycle count.

in Fig. 5b and Fig. S7†), and only a small amount of O-related dislocation clusters appeared, which is in agreement with the above discussion. By utilizing the S and n values at room temperature, the effective mass (m_d^*) was determined and compared with the literature data in Fig. 5d.[22,14] The m_d^* values of BTS ($\sim 1.0m_0$) are almost the same as the previously reported n-type BT-based materials. For sample S10, the m_d^* value increases to $\sim 1.2m_0$ due to the slightly increased electron concentration (5.3×10^{19} cm^{-3}). As discussed above, the observed variation of electron concentration is mainly ascribed to the donor-like effect of the O-related dislocation clusters. As predicted, small m_d^* values of the samples with thick ALD coating could be mainly attributed to the formation of large-scale Bi_2O_x precipitates. To enhance TE performance, an increased ratio of carrier mobility (μ) to κ_{latt}, along with a high m_d^*, is required, which could be estimated by the parameter $\mu(m_d^*/m_0)^{3/2}/\kappa_{latt}$ (Fig. 5e). The $\mu(m_d^*/m_0)^{3/2}/\kappa_{latt}$ value sharply increased from 40.1×10^{-3} K m^3 V^{-1} S^{-1} W^{-1} for pure BTS to 52.2×10^{-3} K m^3 V^{-1} S^{-1} W^{-1} for S10, and then gradually decreases to 27.5×10^{-3} K m^3 V^{-1} S^{-1} W^{-1} for S90. The transition of the scattering mechanism from phonon-dominated to more impurity-dominated transport behavior caused by the high-density O-related dislocation clusters is essential for achieving a high $\mu(m_d^*/m_0)^{3/2}/\kappa_{latt}$ value of S10. Thus, decoupling the three key thermoelectric parameters and simultaneously modifying all of them toward the desired direction has been achieved in BTS by introducing high-density O-related dislocation clusters using the ALD-based solid phase diffusion strategy.

Due to the substantially enhanced power factor and suppressed κ_{latt} by introducing O-related dislocation clusters, the figure of merit ZTs were significantly enhanced, as shown in Fig. 4f. Among these, S10 exhibits the highest ZT of 0.91 at 430 K, which is ~40% higher than that of pristine BTS. Compared with other n-type BT-based nanostructured TE materials, it is an excellent and highly competitive value near the room temperature range.[10,16,19] Furthermore, the ALD-based defect regulation strategy can be extended to other thermoelectric material systems, which is more advantageous than the traditional method.[39–42] This study is an initial attempt at decoupling the three key thermoelectric parameters and simultaneously modifying all of them toward the desired direction for bulk thermoelectric materials by regulating the O-related dislocation clusters at the atomic scale, which provides insight into the structural design and synthesis of broadly functional hybrid thermoelectric material systems.

Conclusions

In summary, we demonstrate the atomic-scale control of oxygen doping in BTS *via* an ALD-based solid phase diffusion strategy. In the BTS matrix, oxygen doping leads to two main forms, *i.e.* O-related dislocation clusters and nano-scale Bi_2O_x precipitates, respectively, which could be tuned by accurately controlling the thickness of ALD coating at the atomic scale. Decoupling the three key thermoelectric parameters and sim-

ultaneously modifying all of them toward the desired direction has been achieved by regulating oxygen doping in the form of oxygen-related dislocation clusters. Due to the substantially enhanced power factor and suppressed κ_{latt}, a maximum *ZT* of 0.91 is obtained, approximately 1.4 times higher than that of the BTS matrix. This study is an initial attempt at decoupling the three key thermoelectric parameters by atomic-scale tuning of oxygen-doping in BTS, which provides insight into the structural design and synthesis of broadly functional hybrid thermoelectric material systems.

Conflicts of interest

There are no conflicts to declare.

Acknowledgements

The work was financially supported by the National Natural Science Foundation of China (No. 21905007), the Guangdong Key-lab Project (No. 2017B0303010130), the Shenzhen Science and Technology Research (Grant No. JCYJ20150629144612861 and JCYJ20150827155136104). Also, this work was supported by the Pico Center at SUSTech that receives support from the Presidential fund and the Development and Reform Commission of Shenzhen Municipality.

Notes and references

1 H. Zhu, C. Xiao and Y. Xie, *Adv. Mater.*, 2018, **30**, 1802000.
2 L. E. Bell, *Science*, 2008, **321**, 1457–1461.
3 W. G. Zeier, A. Zevalkink, Z. M. Gibbs, G. Hautier, M. G. Kanatzidis and G. J. Snyder, *Angew. Chem., Int. Ed.*, 2016, **55**, 2–18.
4 J. P. Heremans, *Nature*, 2014, **508**, 327–328.
5 M. Beekman, D. T. Morelli and G. S. Nolas, *Nat. Mater.*, 2015, **14**, 1182–1185.
6 L. Hu, H. Wu, T. Zhu, C. Fu, J. He, P. Ying and X. Zhao, *Adv. Energy Mater.*, 2015, **5**, 1500411–1500424.
7 Y. Pei, G. Tan, D. Feng, L. Zheng, Q. Tan, X. Xie, S. Gong, Y. Chen, J.-F. Li, J. He, M. G. Kanatzidis and L.-D. Zhao, *Adv. Energy Mater.*, 2017, **7**, 1601450–1601461.
8 M. Ibáñez, R. Zamani, W. Li, D. Cadavid, S. Gorsse, N. A. Katcho, A. Shavel, A. M. López, J. R. Morante, J. Arbiol and A. Cabot, *Chem. Mater.*, 2012, **24**(23), 4615–4622.
9 M. Ibáñez, D. Cadavid, R. Zamani, N. G. Castelló, V. I. Roca, W. Li, A. Fairbrother, J. D. Prades, A. Shavel, J. Arbiol, A. P. Rodríguez, J. R. Morante and A. Cabot, *Chem. Mater.*, 2012, **24**(3), 562–570.
10 S. Li, T. Fan, X. Liu, F. Liu, H. Meng, Y. Liu and F. Pan, *ACS Appl. Mater. Interfaces*, 2017, **9**, 3677–3685.
11 D. Kong, J. J. Cha, K. Lai, H. Peng, J. G. Analytis, S. Meister, Y. Chen, H.-J. Zhang, I. R. Fisher, Z.-X. Shen and Y. Cui, *ACS Nano*, 2011, **5**, 4698–4703.
12 J. Wu, C. Tan, Z. Tan, Y. Liu, J. Yin, W. Dang, M. Wang and H. Peng, *Nano Lett.*, 2017, **17**, 3021–3026.
13 R. J. Macedo, S. E. Harrison, T. S. Dorofeeva, J. S. Harris and R. A. Kiehl, *Nano Lett.*, 2015, **15**(7), 4241–4247.
14 Y. Pan, Y. Qiu, I. Witting, L. Zhang, C. Fu, J. Li, Y. Huang, F. Sun, J. He, G. J. Snyder, C. Felser and J. Li, *Energy Environ. Sci.*, 2019, **12**(2), 624–630.
15 M. Hong, Z.-G. Chen, L. Yang and J. Zou, *Nanoscale*, 2016, **8**, 8681–8686.
16 C. Zhang, H. Ng, Z. Li, K. A. Khor and Q. Xiong, *ACS Appl. Mater. Interfaces*, 2017, **9**, 12501–12510.
17 A. Soni, Y. Shen, M. Yin, Y. Zhao, L. Yu, X. Hu, Z. Dong, K. A. Khor, M. S. Dresselhaus and Q. Xiong, *Nano Lett.*, 2012, **12**, 4305–4310.
18 G. Zheng, X. Su, X. Li, T. Liang, H. Xie, X. She, Y. Yan, C. Uher, M. G. Kanatzidis and X. Tang, *Adv. Energy Mater.*, 2016, **6**, 1600595.
19 M. Hong, Z. G. Chen, L. Yang and J. Zou, *Nano Energy*, 2016, **20**, 144–155.
20 Y. Liu, Y. Zhang, K. H. Lim, M. Ibáñez, S. Ortega, M. Li, J. David, S. Martí-Sánchez, K. M. Ng, J. Arbiol, M. V. Kovalenko, D. Cadavid and A. Cabot, *ACS Nano*, 2018, **12**(7), 7174–7184.
21 C. Zhang, C. Zhang, H. Ng and Q. Xiong, *China Mater.*, 2019, **62**, 389–339.
22 S. Li, Y. Liu, F. Liu, D. He, J. He, J. Luo, Y. Xiao and F. Pan, *Nano Energy*, 2018, **49**, 257–266.
23 S. Li, X. Liu, Y. Liu, F. Liu, J. Luo and F. Pan, *Nano Energy*, 2017, **39**, 297–305.
24 S. Li, C. Xin, X. Liu, Y. Feng, Y. Liu, J. Zheng, F. Liu, Q. Huang, Y. Qiu, J. He, J. Luo and F. Pan, *Nano Energy*, 2016, **30**, 780–789.
25 Q. Xie, Y.-L. Jiang, C. Detavernier, D. Deduytsche, R. L. V. Meirhaeghe, G.-P. Ru, B.-Z. Li and X.-P. Qu, *J. Appl. Phys.*, 2007, **102**, 083521.
26 G.-M. Kim, S.-M. Lee, G. H. Michler, H. Roggendorf, U. Gösele and M. Knez, *Chem. Mater.*, 2008, **20**, 3085–3309.
27 M. Reiners, K. Xu, N. Aslam, A. Devi, R. Waser and S. H. Eifert, *Chem. Mater.*, 2013, **25**, 2934–2943.
28 H. Bando, K. Koizumi, Y. Oikawa, K. Daikohara, V. A. Kulbachinskii and H. Ozaki, *J. Phys.: Condens. Matter*, 2000, **12**, 5607–5616.
29 M. Hong, T. C. Chasapis, Z.-G. Chen, L. Yang, M. G. Kanatzidis, G. J. Snyder and J. Zou, *ACS Nano*, 2016, **10**(4), 4719–4727.
30 C. Zhang, M. Mata, Z. Li, F. J. Belarre, J. Arbiol, K. A. Khor, D. Poletti, B. Zhu, Q. Yan and Q. Xiong, *Nano Energy*, 2016, **30**, 630–638.
31 Y. Pan, U. Aydemir, J. A. Grovogui, I. T. Witting, R. Hanus, Y. Xu, J. Wu, C.-F. Wu, F.-H. Sun, H.-L. Zhuang, J.-F. Dong, J.-F. Li, V. P. Dravid and G. J. Snyder, *Adv. Mater.*, 2018, **30**, 1802016.
32 B. Zhu, Z.-Y. Huang, X.-Y. Wang, Y. Yu, L. Yang, N. Gao, Z.-G. Chen and F.-Q. Zu, *Nano Energy*, 2017, **42**, 8–16.
33 F. D. Rosi, *Solid-State Electron.*, 1968, **11**, 833.

34 J. Suh, K. M. Yu, D. Fu, X. Liu, F. Yang, J. Fan, D. J. Smith, Y.-H. Zhang, J. K. Furdyna, C. Dames, W. Walukiewicz and J. Wu, *Adv. Mater.*, 2015, **27**, 3681–3686.
35 J.-H. Bahk and A. Shakouri, *Appl. Phys. Lett.*, 2014, **105**, 052106.
36 R. Kim and M. S. Lundstrom, *J. Appl. Phys.*, 2011, **110**, 034511.
37 L. Hu, H. Wu, T. Zhu, C. Fu, J. He, P. Ying and X. Zhao, *Adv. Energy Mater.*, 2015, **5**, 1500411.
38 W. S. Liu, Q. Y. Zhang, Y. C. Lan, S. Chen, X. Yan, Q. Zhang, H. Wang, D. Z. Wang, G. Chen and Z. F. Ren, *Adv. Energy Mater.*, 2011, **1**, 577.
39 Y. Yu, D.-S. He, S. Zhang, O. C. Mirédinc, T. Schwarz, A. Stoffers, X. Wang, S. Zheng, B. Zhu, C. Scheu, D. Wu, J. Q. He, M. Wuttig, Z. Y. Huang and F. Q. Zu, *Nano Energy*, 2017, **37**, 203–213.
40 L. Hu, Y. Zhang, H. Wu, Y. Liu, J. Li, J. He, W. Ao, F. Liu, S. J. Pennycook and X. Zeng, *Adv. Funct. Mater.*, 2018, **28**, 1803617.
41 W. Li, M. Ibáñez, R. R. Zamani, N. G. Castelló, S. Gorsse, D. Cadavid, J. D. Prades, J. Arbiol and A. Cabot, *CrystEngComm*, 2013, **15**, 8966–8971.
42 M. Ibáñez, R. Zamani, S. Gorsse, J. Fan, S. Ortega, D. Cadavid, J. R. Morante, J. Arbiol and A. Cabot, *ACS Nano*, 2013, **7**(3), 2573–2586.